AIAA SciTech Forum
11–15 & 19–21 January 2021, VIRTUAL EVENT
AIAA Scitech 2021 Forum

10.2514/6.2021-1200

A Low-Cost Aero-Propulsive Analysis of Distributed Electric Propulsion Aircraft

Racheal M. Erhard*, Matthew A. Clarke†, and Juan J. Alonso‡
Stanford University, Stanford, CA, 94305

Despite the complex aero-propulsive interactions inherent in propeller-driven aircraft, low-cost methods for the analysis of distributed electric propulsion (DEP) aircraft are highly desirable to enable rapid aircraft design at the conceptual level. In this paper, a computationally-inexpensive method for analyzing the effect of a wing wake on the performance of pusher propellers is demonstrated using a vortex lattice method (VLM) augmented with boundary layer corrections and coupled with a blade element model (BEM). This approach captures important features in blade loading unattainable by inviscid methods, and at computational costs far below those of high-fidelity methods. The analysis for tractor-configured aircraft uses a vortex ring model to analyze the slipstream interaction of the propellers over the wing. These aero-propulsive analyses are subsequently used to compare performance of comparable pusher- and tractor-configured aircraft. Results show increased propulsive efficiency for individual pusher propellers of up to 16.2%, depending on propeller location and thrust level. At the vehicle level, the DEP aircraft in a pusher configuration benefited from increased aero-propulsive efficiency of 5.5%. An equivalent DEP tractor configuration showed a comparable improvement of 5.3%. The simplicity of this approach allows for fast design iteration of DEP aircraft at a fraction of the cost of current high-fidelity methods.

Nomenclature

$b_{1/2}$	=	wake half-width	V_a	=	axial velocity at propeller
c	=	wing chord	V_t	=	tangential velocity of propeller
$C_{m,n}$	=	influence coefficient matrix of the wing	V_∞	=	freestream velocity
$C_{m_{r,t}}$	=	influence coefficient matrix of vortex rings	W_0	=	maximum velocity deficit at centerline of wake
D	=	drag force	x_{te}	=	distance behind wing trailing edge
D_{iso}	=	isolated vehicle drag	z_{te}	=	vertical distance from wing
I	=	number of propellers	α	=	angle of attack
L	=	lift force	η_p	=	individual propeller efficiency
N	=	number of panels on lifting surface	η_{tot}	=	overall propulsive efficiency
Q	=	torque	Γ_n	=	vortex strength corresponding to panel n
Re_c	=	Reynolds number based on chord	θ_{te}	=	momentum thickness at wing trailing edge
T	=	thrust			

I. Introduction

Propeller-driven aircraft have proven to be the most efficient design solutions for flight at low to mid speeds, making them especially practical for small to mid-sized business aircraft and general aviation. Further performance enhancements can be gleaned by strategic placement and distribution of propellers. For aircraft in a tractor configuration, as in Figure 1a, the propeller slipstream interaction with the wing has been well-studied and shown to improve aerodynamic performance through increased lift and delay of turbulent separation [1–3]. The alternative pusher configuration, as in Figure 1b, offers several potential benefits that are unrealizable by the traditional tractor configuration. First, with the absence of the propeller slipstream over the wing, the pusher configuration can allow for larger regions of laminar

*Ph.D. Candidate, Department of Aeronautics & Astronautics, AIAA Student Member.
†Ph.D. Candidate, Department of Aeronautics & Astronautics, AIAA Student Member.
‡Vance D. and Arlene C. Coffman Professor, Department of Aeronautics & Astronautics, AIAA Associate Fellow.

flow to develop across the wing, which could lead to drag reductions and higher aerodynamic efficiency of the aircraft. The pusher configuration can also benefit from thrust and efficiency enhancements, taking advantage of the wingtip vortices for improved propeller performance [3, 4]. Additionally, by mounting the propellers behind the wing, pilots can experience improved visibility and passengers can benefit from a reduction in cabin noise. To compare potential benefits in an aircraft design environment, it is necessary to first understand the complex aero-propulsive interactions of each configuration type.

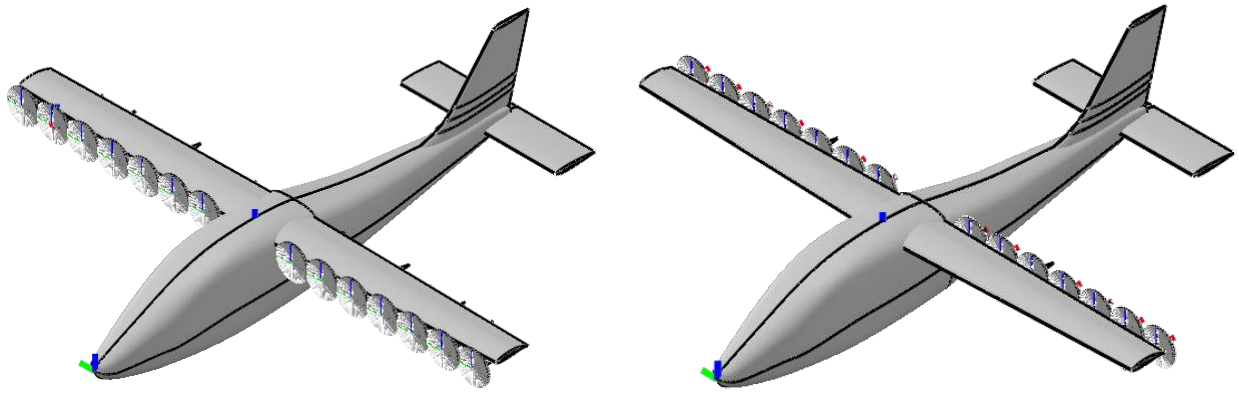

(a) Tractor configuration. **(b) Pusher configuration.**

Fig. 1 Propeller configurations on aircraft wing.

A. Pusher Configuration

The wing-induced velocity field at a downstream propeller changes the blade loading and performance from that of a propeller in a uniform freestream flow. This effect has previously been shown through inviscid theory to increase efficiency, as the propeller recovers vortex energy shed from the wingtips [3]. Experimental results have corroborated this, showing increased propeller thrust and reduced induced drag for such configurations [5]. Stokkermans et al. performed Reynolds-Averaged Navier Stokes (RANS) simulations of a wing with a lifting-line-based propeller model, finding improvements in propeller efficiency for tip-mounted propellers [4]. In this study they compared the propeller performance to that of an isolated propeller, noting a 16% improvement in propulsive efficiency for a propeller contributing 5% of total thrust required for cruise. Further accuracy has been obtained by using unsteady RANS simulations to capture the aero-propulsive interactions. This was done by Yin et al. to evaluate the thrust loading on a pusher propeller and demonstrate the impact that nonuniform loading can have on acoustics [6]. The aerodynamic analysis in their study required 25 days of wall-clock run time for 16 propeller rotations using 96 CPUs. Although a high level of detail in the physics of this model was achieved, the computational runtime makes such an approach impractical for design at the conceptual level.

B. Tractor Configuration

Propeller wakes have previously been modeled using vortex tube models [7], which have been used with wings modeled by lifting line theory or panel methods to evaluate the slipstream effect [8]. More accurate propeller models capture both the tangential and axial induced velocities. McVeigh et al. [9] and Stone [10] applied results from a blade element momentum theory (BEMT) analysis of the propeller to a modified lifting-line model and a fixed-wake panel method, respectively. In these approaches, the mutual interaction between the propeller and the wing was neglected. These interdependencies were captured by Veldhuis [11] and Witkowski et al. [12] through the use of a vortex-lattice method (VLM) modeling both the propeller and the wing with close agreement to experimental tests. Higher-fidelity models that remove the inviscid and irrotational assumption have also been studied [13–17]. Although such methods may model the physics of the propeller–wing interaction more accurately, the computational cost associated with mesh generation, large matrix inversion to solve for state variables, and post-processing limits their application to single design point conditions. As a result, relaxing the fixed wake assumption in potential flow methods, such as that by Bramesfeld and Maughmer [18] which was later applied to a propeller-wing system by Cole et al. [19], is more tractable for aircraft design at the conceptual level.

C. Research Objectives

Inviscid methods for modeling aero-propulsive interactions provide reasonable approximations for conceptual design, however, such inviscid models are unable to capture important blade loading features on aft-mounted propellers obtained through viscous modeling of the wing-propeller interaction. High-fidelity methods allow for increased accuracy in the prediction of propeller and wing interactions, but at significant computational expense. This proves challenging in conceptual design, where designers require evaluation of numerous configurations, and at different operating conditions, as opposed to a single-point analysis. With this in mind, the key objectives of this paper are as follows:

1) Develop a computationally-inexpensive method for appropriately modeling the aero-propulsive interactions of both pusher- and tractor-configured aircraft.
2) Evaluate the effect of distributed electric propulsion on overall vehicle performance of comparable tractor and pusher configurations in cruise.

In this paper, we tackle the challenge of accurately modeling propeller-wing interactions at low-cost. The paper is organized as follows: in Section II we discuss the wing and propeller models developed to enable appropriate analysis of these interactions. In Section III we present the vehicle configurations we will use to compare performance. Section IV provides our results, first for an individual propeller operating in the wake of the wing, and second for the DEP aircraft in pusher- and tractor-configurations. We then end with our conclusions and a discussion of future work in Section V.

II. Approach

The wing analysis includes a blown wing slipstream analysis for tractor-configured propellers, as well as a wing wake analysis to compute the velocity field at the plane of downstream propellers. The propeller analysis, based on blade element theory, is used to evaluate propeller performance, and accounts for the wing wake for aft-mounted propellers. The aero-propulsive efficiency is then used to compare the vehicle-level performance of different aircraft configurations.

A. Wing Analysis

Several low-fidelity methods exist for determining the aerodynamic forces and velocity field produced by a wing. The vortex lattice method (VLM) is an example of such a method with high accuracy and reduced complexity, and has been developed in SUAVE, an open-source aircraft design environment. It begins by discretizing the wing into a lattice of chordwise and spanwise panels, each containing a horseshoe vortex as in lifting-line theory. Using the Biot-Savart law, the velocities induced by all horseshoe vortices at each control point located at the three-quarter chord of each panel are computed, yielding an influence coefficient matrix. Applying flow tangency along the camberline, the vortex strengths are determined for the given geometry and flight conditions. These vortex strengths are used to compute the aerodynamic forces on the wing, and can also be used to compute induced velocities elsewhere in the flow, again using the Biot-Savart law. The implementation of the VLM in SUAVE uses a drag-free wake, where the trailing vortex legs leave the trailing edge of the wing as straight segments extending downstream and parallel to the freestream. It is assumed that the flow remains attached without separation along the wing.

1. Wing Wake Analysis

The velocity field downstream of the wing is required for the analysis of a pusher-configured propeller. The inviscid wing wake is computed by leveraging the vortex strengths solved for previously by the VLM at the given flight condition. First, a new influence coefficient matrix is computed for a set of new control points located in the propeller plane downstream of the wing. To avoid discontinuities introduced by the singularities of the trailing vortices, these new control points are selected to lie between trailing vortex lines. The velocity at each new control point, m, in the propeller plane is then computed using the vector of vortex strengths from the VLM and the new influence coefficient matrix:

$$\vec{v}_m = \sum_n \vec{C}_{m,n}\Gamma_n. \tag{1}$$

The resulting inviscid velocity field is then augmented with the velocity deficit due to the boundary layer growth along the wing. The velocity deficit behind a flat plate follows the exponential relation of Equation 2 [20], which is used to approximate the velocity deficit in the propeller plane behind thin wings at small angles of attack:

$$\frac{V_{deficit}}{W_0} = exp\left(-2.773\left(\frac{z_{te}}{b_{1/2}}\right)^2\right). \tag{2}$$

The maximum velocity deficit, W_0, and wake half-width, $b_{1/2}$, follow the one-half power laws [20]:

$$\frac{W_0}{V_\infty} = \left(0.402\frac{x_{te}}{\theta_{te}}\right)^{-1/2}, \tag{3}$$

$$\frac{b_{1/2}}{\theta_{te}} = \left(0.355\frac{x_{te}}{\theta_{te}}\right)^{1/2}. \tag{4}$$

Here, x_{te} is the distance behind the trailing edge of the wing, θ_{te} is the momentum thickness at the trailing edge, and z_{te} is the vertical distance from the trailing edge of the wing. With the flow tripped at the leading edge, the turbulent boundary layer develops, and the trailing edge momentum thickness is approximated as that of a flat plate:

$$\theta_{te} = \frac{0.036c}{Re_c^{0.2}}. \tag{5}$$

Figure 2 shows the inviscid wake velocities and the velocity deficit due to the viscous contribution for several cases of $\frac{x_{te}}{\theta_{te}}$. The downwash shown in Figure 2a is as expected, with larger downwash near the wingtips and upwash just outside of the wingtips. The inviscid axial velocity in Figure 2b also aligns with expectations when considering the contribution of the bound vortices, and is seen to be of lower magnitude than the downwash. From Figure 2c it is clear that the viscous contribution to the wake is reduced for smaller trailing edge momentum thickness, or larger distance from the trailing edge. This matches experimental results by Chevray and Kovasznay [21].

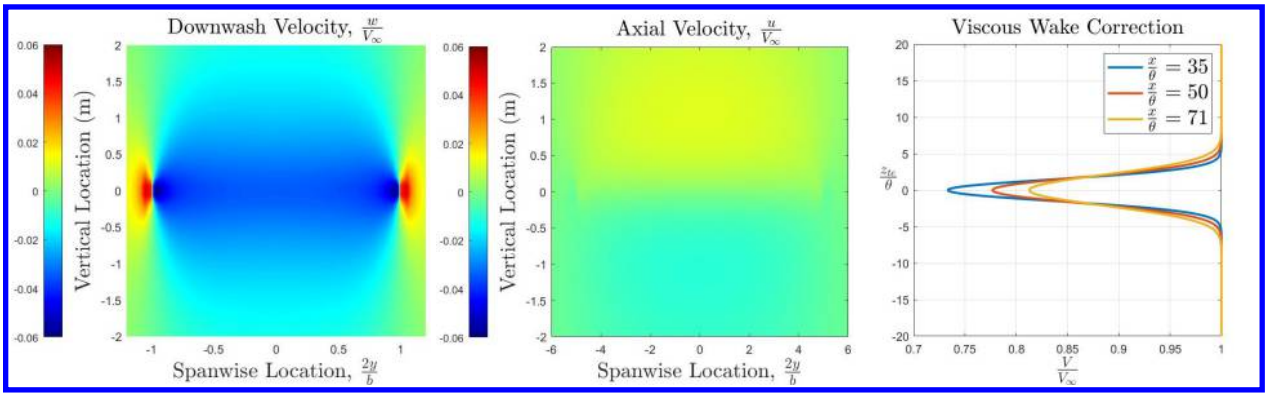

(a) Inviscid downwash in wing wake. **(b) Inviscid axial velocity in wing wake.** **(c) Viscous wake addition.**

Fig. 2 Velocity field in wing wake.

2. Propeller Slipstream Analysis

A vortex ring model similar to that used by Patterson and German [22] is used to model the effect of the propeller slipstream on the wing of the tractor configuration. This concept of representing vorticity as rings closely follows Helmholtz's vortex theorems, which state that the strength of a vortex filament is constant and must end at a boundary, extend to infinity, or in this case, form a closed loop. The geometry of each ring depends on the fixed helical wake shape, modeled in Figure 3b, and its corresponding vortex strength from the BEM. As the propeller rotates about its axis at each predefined time step, a distribution of circulation can be determined from the load on the propeller blades. Slipstream contraction of the helical wake is modeled using the approach outlined by Stone [10]. Realistically, the uniform helical shape of the wake breaks down due to instability, leapfrogging, and pairing of tip vortex filaments as noted by Alvarez [23]. However, in the first few rotations where the assumptions of momentum theory are valid, a fixed wake approximation is reasonable for determining the aerodynamic loads. For the given flight conditions, 100 time steps of wake development was sufficient to achieve such definition. With a method that uses the same singularities as the horseshoe vortices of the VLM, the induced velocity created by the potential of the wake can be computed anywhere in the flow field.

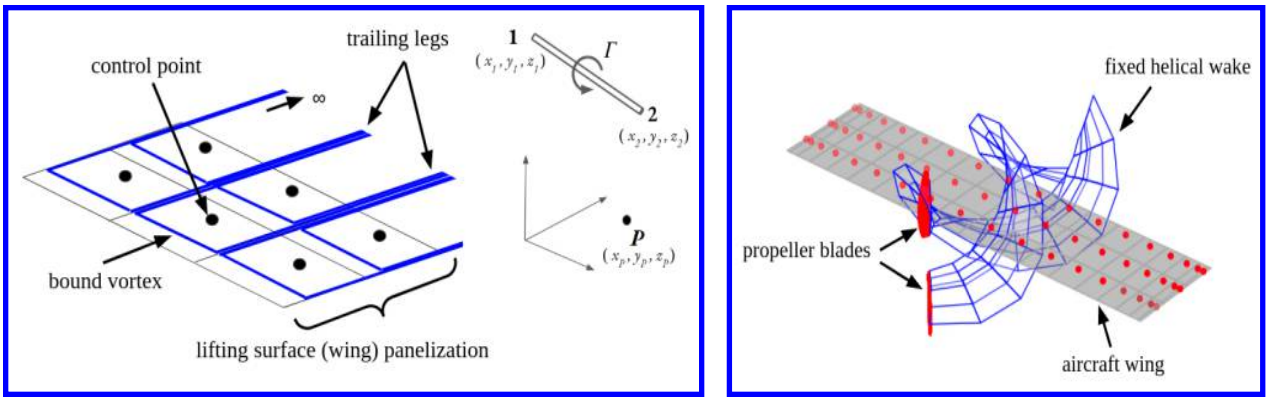

(a) Schematic of VLM wing parametization and influence of a vortex line segment at point P.

(b) Fixed helical wake model superimposed on wing lattice.

Fig. 3 Visualization of potential methods for prediction of aero-propulsive loads.

The vortex ring elements are planar and trapezoidal in shape with a finite chord and consist of vortex filaments of equal strength on all four sides. The total induced velocity of each ring is computed by summing the influence from the four individual filaments. For the vortex line segment between points 1 and 2 in Figure 3a, the velocity induced at an arbitrary point, P can be determined by Equation 6,

$$\vec{v}_{1,2} = \frac{\Gamma}{4\pi} \frac{\vec{r}_1 \times \vec{r}_2}{|\vec{r}_1 \times \vec{r}_2|^2} \vec{r}_0 \cdot \left(\frac{\vec{r}_1}{r_1} - \frac{\vec{r}_2}{r_2} \right), \tag{6}$$

where

$$\vec{r}_0 = \sqrt{(x_2 - x_1)^2 + (y_2 - y_1)^2 + (z_2 - z_1)^2}, \tag{7a}$$

$$\vec{r}_1 = \sqrt{(x_p - x_1)^2 + (y_p - y_1)^2 + (z_p - z_1)^2}, \tag{7b}$$

$$\vec{r}_2 = \sqrt{(x_p - x_2)^2 + (y_p - y_2)^2 + (z_p - z_2)^2}. \tag{7c}$$

Therefore,

$$\vec{v}_{ring} = \vec{v}_{AB} + \vec{v}_{BC} + \vec{v}_{CD} + \vec{v}_{DA}. \tag{8}$$

Note that continuity is preserved by the order of the subscripts, which indicate the direction of the circulation vector. The total induced velocity at a control point on the wing, denoted by m, can be determined by numerically integrating the collective influence from the system of vortex rings from the propeller and the system of horseshoe vortices on the wing as provided in Equation 9,

$$\vec{v}_{m_{tot}} = \vec{v}_{m_{wing}} + \vec{v}_{m_{wake}}, \tag{9}$$

where

$$\vec{v}_{m_{wing}} = \sum_{n=1}^{N} \vec{C}_{m,n} \Gamma_n, \tag{10a}$$

$$\vec{v}_{m_{wake}} = \sum \vec{C}_{m_{r,t}} \Gamma_r. \tag{10b}$$

N is the total number of panels on the lifting surface. $\vec{C}_{m,n}$ is the influence coefficient matrix which depends on the geometry of the nth horseshoe vortex and its distance from the control point of the mth panel. The construction of these matrices for the VLM is outlined in [24]. Similarly, $\vec{C}_{m_{r,t}}$ is the influence matrix constructed from the distribution of vortex rings in the helical wake at radial location, r, and time step, t.

B. Propeller Analysis

Blade-element models (BEMs) are commonly used for analyzing propeller performance in axial flight due to their computational efficiency and relative accuracy [25–29]. The BEM developed in SUAVE divides each blade into radial sections and computes the effective angle of attack of each blade section at each azimuthal location. The effective angle of attack depends on the twist angle of the blade as well as the axial and tangential velocity components at the section location. Once this is established, the lift and drag of each two-dimensional section of the blade is computed, and the sectional forces are decomposed into corresponding thrust and torque forces at each azimuthal location. For propellers in a non-uniform freestream flow, the thrust and torque forces are time-averaged around the azimuth before summing across the blade to provide a measure of total thrust and torque of the propeller, as well as the time-averaged propeller efficiency.

C. Aircraft-Level Analysis

For the pusher-configured aircraft, the propeller effect on the wing is relatively small and is therefore neglected. This approximation is reasonable for propellers located far enough behind the wing or operating at sufficiently-low thrust levels [30, 31]. The latter is particularly relevant for DEP aircraft, where the thrust is distributed across the span. For the tractor-configured aircraft, the wing effect on the propeller is also relatively small and thus neglected. For both configurations, the wing angle of attack and propeller advance ratios are optimized to converge on a level and steady flight condition. The resulting aerodynamic and propulsive efficiencies are then used in the computation of an aero-propulsive efficiency, given by Equation 11, to assess and compare the vehicle-level performance of different configurations:

$$\left(\frac{L}{D}\right) \cdot \eta_{tot}. \tag{11}$$

Here, η_{tot} is the total propulsive efficiency of the propellers, and is related to the individual propulsive efficiencies of the I distributed propellers by Equation 12:

$$\eta_{tot} = \frac{VT}{P_{tot}} = \sum_{i=1}^{I} \frac{P_i}{P_{tot}} \eta_{p,i}. \tag{12}$$

III. Vehicle Setup

A general aviation aircraft inspired by the X-57 Maxwell is shown in pusher and tractor configurations in Figure 1 and is used to evaluate the effect of distributed electric propulsion on aero-propulsive efficiency. The main wing has a taper ratio of 0.7 with a 9.6m span. Direct comparisons between tractor- and pusher- configured DEP are explored using three variants of propeller distributions. Fourteen-, ten-, and six-propeller DEP models are used in both pusher and tractor configurations. The sizes of the propellers were chosen to allow for equal spacing between propeller tips across all configurations, and are shown in Table 1. Before analyzing the wing and propeller interactions, the isolated drag of the aircraft in cruise was computed and provides baseline thrust values required per propeller as also shown in Table 1. For the pusher configuration, since the propeller effect on the wing is neglected, the baseline thrust becomes the actual thrust required by each propeller for steady and level flight. The advance ratio of the propeller is then optimized to converge on this thrust. For the tractor configuration, the baseline thrust provides an initial point used to converge on steady and level flight through an optimization of the wing angle of attack and the advance ratio of the propeller.

Table 1 Propeller parameters for each distribution case.

Propeller Parameters		
Propeller Distribution (Number of Propellers)	Tip Radius (m)	Baseline Thrust (N, Per Propeller)
14	0.31	24 (7% D_{iso})
10	0.45	34 (10% D_{iso})
6	0.77	57 (17% D_{iso})

IV. Results

A. Individual Propeller in Pusher Configuration

A 0.45m radius propeller is first used to evaluate the performance of an individual pusher propeller in the wake of the wing. The axial and downwash velocity fields produced by the wing wake at the propeller disk are extracted from the wake model, and are used to obtain the axial and tangential velocities shown in Figure 4. The downwash from the wing generates an increased tangential velocity of the propeller on the upward rotation. The boundary layer effect from the wing yields a significant axial velocity deficit in a thin region downstream of the wing. Small changes in axial velocity from the freestream are seen outside of this region due to the influence of the bound vortices along the wing.

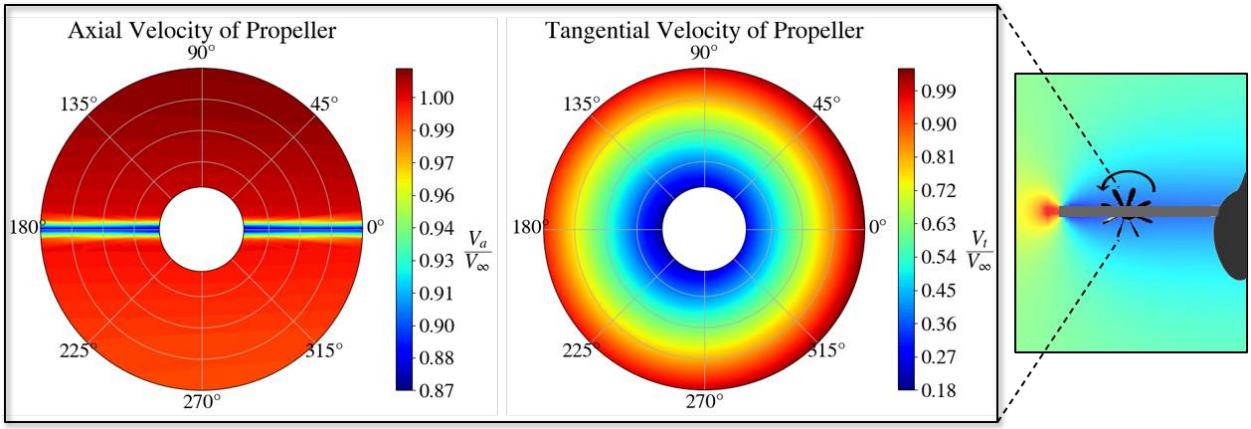

Fig. 4 Velocities at propeller location.

With the wing effect accounted for in the propeller model, the increased tangential velocities on the right half of the propeller disk result in higher lift and correspondingly higher thrust and torque outputs. This is seen by the regions of increased thrust and torque on the right half of the propeller disks in Figure 5.

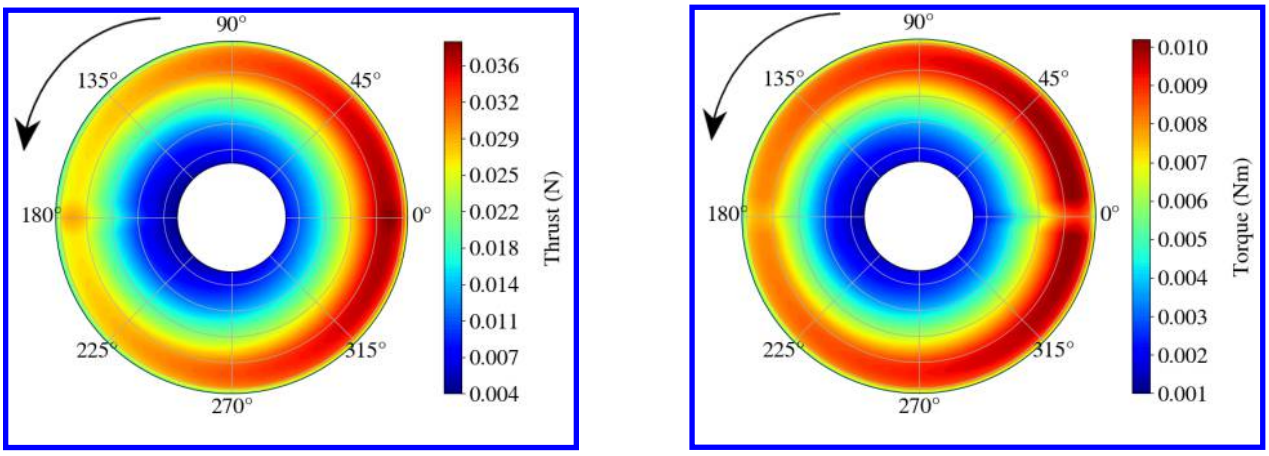

(a) Thrust distribution. **(b) Torque distribution.**

Fig. 5 BEM output blade loading distribution.

A critical feature of the thrust distribution in Figure 5a is the region of increased thrust encountered as the blade passes through the 0° and 180° azimuthal angles. In these regions the blade encounters a 13% reduction in axial velocity, seen in Figure 4, due to the viscous boundary layer contribution to the wing wake. This velocity deficit increases the effective angle of attack of the blade and tilts the lift vector into the thrust direction, resulting in these high thrust areas. These blade loading trends match the unsteady RANS results found by Yin et al. [6] at a fraction of the cost, taking just 25 seconds for the full wing wake and propeller analyses as opposed to the 25 days required for the URANS model.

Although this low-fidelity method will not capture the physics as well as a full unsteady RANS simulation, it does capture the major trends with the critical regions of increased thrust behind the wing, which will correspond to increased noise due to the high thrust gradient. Capturing this feature is promising, and could enable the incorporation of acoustic considerations into aircraft conceptual design, as we intend to do in future work.

The effect of the wing wake on propulsive efficiency depends largely on the strength of the wingtip vortices, and the proximity of the propeller to the wingtips. Figure 6 demonstrates these effects on the propulsive efficiency of the individual propeller, η_p, as well as its weighted contribution, $\eta_p \times \%D_{iso}$, where D_{iso} is the isolated drag of the vehicle at the given flight condition. Maximum benefits in individual propeller efficiency are achieved as the propeller moves towards the wingtip. Although the lower thrust levels show higher increases in individual propulsive efficiency during cruise, as shown in Figure 6a, the larger thrust levels perform better when considering their impact at the vehicle-level, as demonstrated in Figure 6b. Figures 6c and 6d show that at higher angles of attack, which will be encountered during climb segments, the propeller benefits further from the high vortex strengths produced, resulting in significant improvements to individual propeller efficiencies of up to 24% for a propeller providing a thrust of 5% D_{iso}.

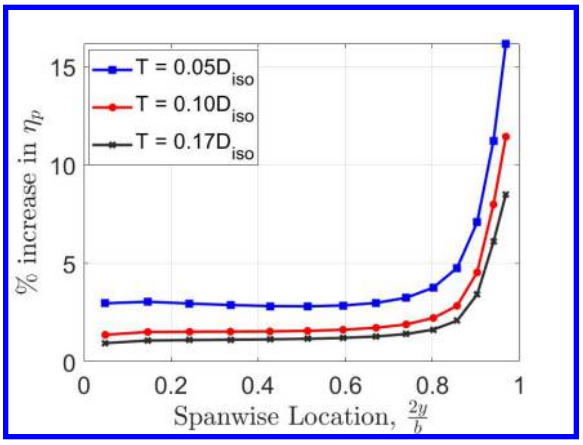

(a) Effect of propeller location on efficiency at cruise conditions.

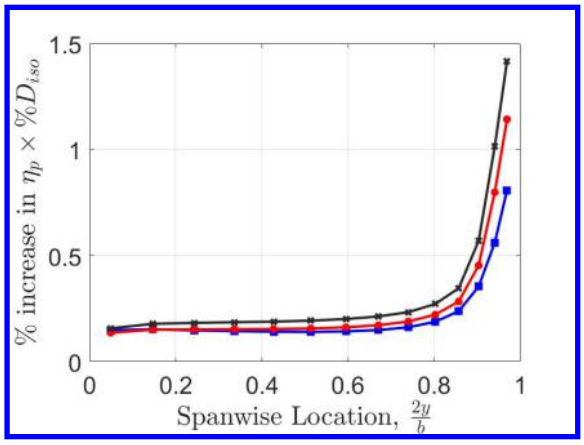

(b) Effect of propeller location on weighted efficiency at cruise conditions.

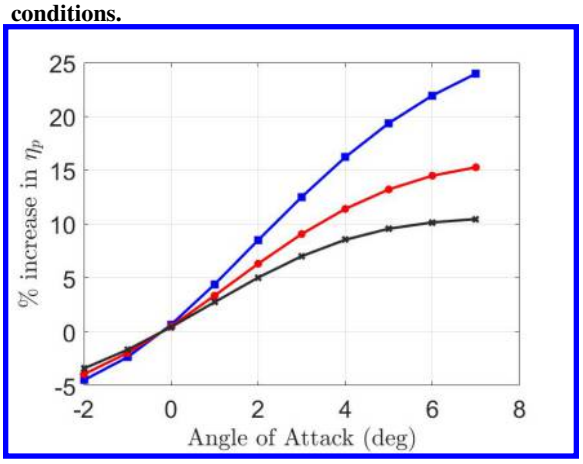

(c) Effect of angle of attack on propeller efficiency.

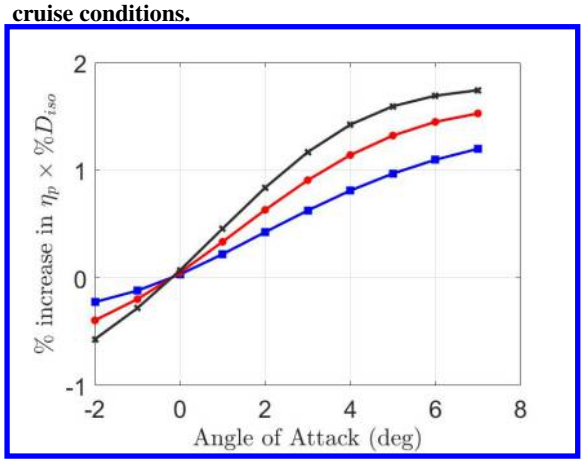

(d) Effect of angle of attack on weighted efficiency.

Fig. 6 Effect of spanwise location, angle of attack, and thrust level on individual propeller performance.

For a given thrust level, a larger propeller radius was found to increase the propulsive efficiency of the individual propeller at all locations along the span, as shown in Figure 7a. The previous results incorporated an inboard-up rotation with the propellers rotating against the direction of the wingtip vortices. It is important to note that for an inboard-down rotation the opposite trends result, as shown in Figure 7b for the 5% D_{iso} thrust level. One implication of this is that the benefits of tip-mounted propellers are likely restricted to electric propulsion aircraft, since engine manufacturers are unlikely to produce two internal combustion engines that rotate in opposite directions.

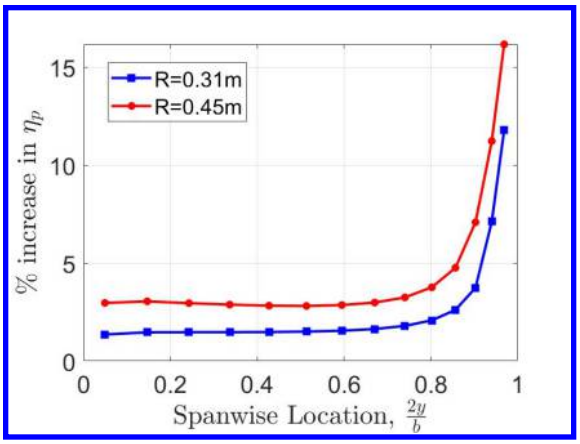

(a) Effect of propeller radius on efficiency improvement for $T = 0.05D_{iso}$.

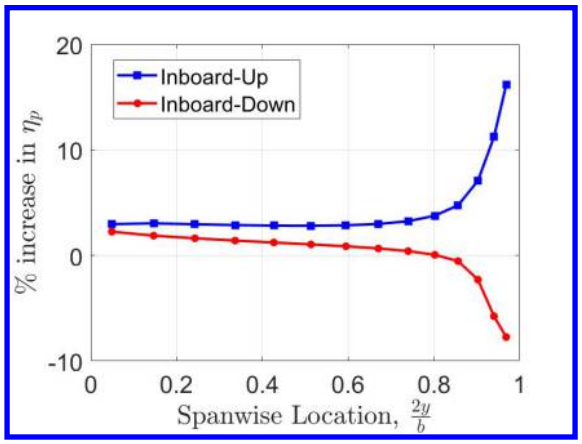

(b) Effect of rotation direction on efficiency improvement for $T = 0.05D_{iso}$.

Fig. 7 Effect of propeller radius and rotation direction on efficiency improvement.

B. DEP Aircraft Configurations

For the propeller sizing provided in Table 1, the three DEP aircraft in the pusher configuration were analyzed. As shown in the prior results, the larger propeller operating at a lower thrust level sees the highest improvement in propulsive efficiency. This introduces competing effects in the DEP pusher configurations, where increasing the size of the propeller reduces the number of propellers along the span, thereby increasing the thrust level required by each propeller for cruise. For the three distributions considered here, the increase in propeller efficiencies of the individual propellers at their fixed thrust values are shown in Figure 8a. The 6-propeller configuration with the largest radius yields higher increases in propeller efficiency across the span despite having a higher thrust level per propeller. The total propulsive efficiency was computed using Equation 12, and combined with the lift-to-drag ratio to provide a measure of aero-propulsive efficiency. The DEP tractor configurations were then analyzed with the same propeller spanwise locations. A comparison of the aero-propulsive efficiencies of the tractor and pusher configuration for each propeller distribution case is shown in Figure 8b.

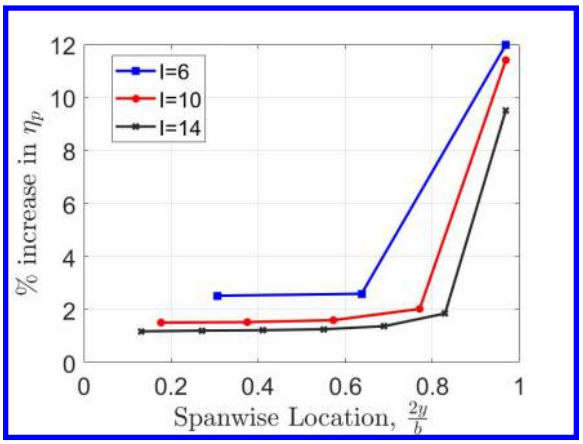

(a) Propeller efficiencies for pusher configurations.

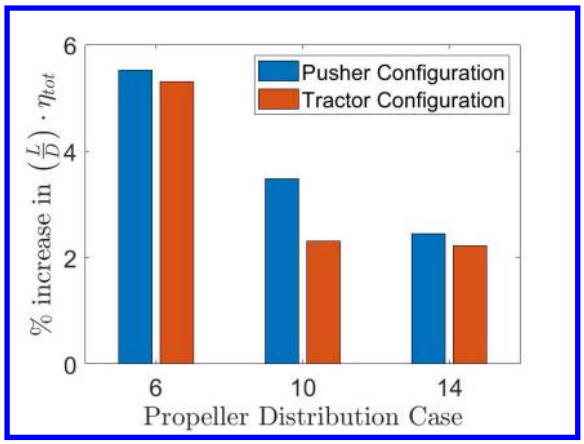

(b) Comparison of aero-propulsive efficiencies.

Fig. 8 Performance comparison of DEP Aircraft Configurations.

For the three distributions, similar performance enhancements over the isolated cases are achieved with either a pusher or tractor configuration. This follows Kroo's conclusion that for an inviscid analysis, equal increases in efficiency can be obtained by using tractor or pusher configurations [3]. Although the viscous component of the wake analysis in our method is important for capturing the blade loading characteristics that match high-fidelity methods, its contribution to the increase in propulsive efficiency is relatively small, and thus the inviscid wake contribution dominates the

performance trends.

These results show the successful implementation of the aero-propulsive analyses developed in this paper applied to three specified cases of pusher- and tractor-configured DEP aircraft. The purpose of this paper was to demonstrate the ability to model the aero-propulsive interactions at low computational cost, and use these models to compare DEP aircraft configurations. The results in Figure 8b are therefore not intended to provide an indication of optimal propeller distribution, but rather to show the direct comparison between three specified propeller distribution cases in both pusher and tractor configuration. Future applications can extend this work to further measure the performance benefits of propeller distributions by performing a full vehicle optimization.

V. Conclusion

In this paper, a comprehensive aero-propulsive method for the analysis of DEP aircraft was developed and used to evaluate the aero-propulsive efficiency of a general aviation aircraft under various propeller distributions. The approach included the implementation of a generalized wing analysis using a vortex lattice method and a generalized propeller analysis using blade element theory. Additional analyses of the propeller slipstream, using a vortex ring model, and the wing wake velocity field, using the VLM with boundary layer corrections, enabled proper modeling of the propeller-wing interactions for both pusher- and tractor-configured aircraft.

For an individual propeller in pusher configuration, results corroborated prior findings that high vortex strengths near the wingtips lead to increased propulsive efficiency of the inboard-up rotating propeller. Inclusion of the wing boundary layer effect in the computation of the velocity field downstream of the wing allowed for capturing blade loading features that match trends obtained from high-fidelity methods. These features are critical when it comes to predicting noise, which is directly impacted by the gradient of thrust loading, and may enable acoustic considerations to be incorporated at low computational cost in future conceptual aircraft design. The aero-propulsive loads from medium-fidelity tools such as those employed in this study can therefore provide time histories of varying loads used in sound propagation formulations such as the Ffowcs Williams-Hawkings equation, as we intend to explore in future work.

Finally, the analysis of comparable pusher- and tractor-configured aircraft showed similar gains in aero-propulsive efficiency over their respective isolated cases. Now that this analysis framework is in place, a full optimization of DEP aircraft can be conducted to provide meaningful analysis of the effect of an optimal propeller distribution on overall vehicle efficiency, and at a significant reduction in computational expense.

References

[1] Catalano, F., "On the effects of an installed propeller slipstream on wing aerodynamic characteristics," *Acta Polytechnica*, Vol. 44, No. 3, 2004.

[2] Stoll, A. M., Bevirt, J., Moore, M. D., Fredericks, W. J., and Borer, N. K., "Drag reduction through distributed electric propulsion," *14th AIAA Aviation Technology, Integration, and Operations Conference*, 2014, p. 2851.

[3] Kroo, I., "Propeller-Wing Integration for Minimum Induced Loss," *Journal of Aircraft*, Vol. 23, No. 7, 1986.

[4] Stokkermans, T. C., Nootebos, S., and Veldhuis, L. L., "Analysis and Design of a Small-Scale Wingtip-Mounted Pusher Propeller," *AIAA Aviation 2019 Forum*, 2019, p. 3693.

[5] Patterson, J., J, and Bartlett, G., "Effect of a wing-tip mounted pusher turboprop on the aerodynamic characteristics of a semi-span wing," *21st Joint Propulsion Conference*, 1985, p. 1286.

[6] Yin, J., Stuermer, A., and Aversano, M., "Aerodynamic and aeroacoustic analysis of installed pusher-propeller aircraft configurations," *Journal of Aircraft*, Vol. 49, No. 5, 2012, pp. 1423–1433.

[7] Segalini, A., and Alfredsson, P. H., "A simplified vortex model of propeller and wind-turbine wakes," *Journal of Fluid Mechanics*, Vol. 725, 2013, pp. 91–116.

[8] Miranda, L., and Brennan, J., "Aerodynamic effects of wingtip-mounted propellers and turbines," *4th Applied Aerodynamics Conference*, 1986, p. 1802.

[9] McVeigh, M., Gray, L., and Kisielowski, E., *Prediction of span loading of straight-wing/propeller combinations up to stall*, National Aeronautics and Space Administration, 1975.

[10] Stone, R. H., "Aerodynamic Modeling of the Wing-Propeller Interaction for a Tail-Sitter Unmanned Air Vehicle," *Journal of Aircraft*, Vol. 45, No. 1, 2008, pp. 198–210.

[11] Veldhuis, L. L. M., "Propeller Wing Aerodynamic Interference," Ph.D. thesis, Delft Univ. of Technology, Delft, The Netherlands, 2005.

[12] Witkowski, D. P., Lee, A. K., and Sullivan, J. P., "Aerodynamic interaction between propellers and wings," *Journal of Aircraft*, Vol. 26, No. 9, 1989, pp. 829–836.

[13] Gomariz-Sancha, A., Maina, M., and Peace, A. J., "Analysis of propeller-airframe interaction effects through a combined numerical simulation and wind-tunnel testing approach," *53rd AIAA Aerospace Sciences Meeting*, 2015, p. 1026.

[14] Roosenboom, E. W., Stürmer, A., and Schröder, A., "Advanced experimental and numerical validation and analysis of propeller slipstream flows," *Journal of Aircraft*, Vol. 47, No. 1, 2010, pp. 284–291.

[15] Dang, T., "Simulations of propeller/airframe interference effects using an Euler correction method," *Journal of Aircraft*, Vol. 26, No. 11, 1989, pp. 994–1001.

[16] Thom, A., and Duraisamy, K., "Computational Investigation of Unsteadiness in Propeller Wake–Wing Interactions," *Journal of Aircraft*, Vol. 50, No. 3, 2013, pp. 985–988.

[17] Whitfield, D., and Jameson, A., "Euler equation simulation of propeller-wing interaction in transonicflow," *Journal of Aircraft*, Vol. 21, No. 11, 1984, pp. 835–839.

[18] Bramesfeld, G., and Maughmer, M. D., "Relaxed-wake vortex-lattice method using distributed vorticity elements," *Journal of Aircraft*, Vol. 45, No. 2, 2008, pp. 560–568.

[19] Cole, J. A., Maughmer, M. D., Kinzel, M., and Bramesfeld, G., "Higher-order free-wake method for propeller-wing systems," *Journal of Aircraft*, Vol. 56, No. 1, 2019, pp. 150–165.

[20] Ramaprian, B., Patel, V., and Sastry, M., "The symmetric turbulent wake of a flat plate," *AIAA Journal*, Vol. 20, No. 9, 1982, pp. 1228–1235.

[21] Chevray, R., and Kovasznay, L. S., "Turbulence measurements in the wake of a thin flat plate." *AIAA Journal*, Vol. 7, No. 8, 1969, pp. 1641–1643.

[22] Patterson, M. D., and German, B., "Conceptual design of electric aircraft with distributed propellers: Multidisciplinary analysis needs and aerodynamic modeling development," *52nd Aerospace Sciences Meeting*, 2014, p. 0534.

[23] Alvarez, E. J., and Ning, A., "Development of a Vortex Particle Code for the Modeling of Wake Interaction in Distributed Propulsion," *AIAA Applied Aerodynamics Conference*, 2018.

[24] Katz, J., and Plotkin, A., *Low-Speed Aerodynamics*, Vol. 13, Cambridge University Press, 2001.

[25] Gur, O., and Rosen, A., "Comparison between blade-element models of propellers," *The Aeronautical Journal*, Vol. 112, No. 1138, 2008, pp. 689–704.

[26] Jeon, M., Lee, S., and Lee, S., "Unsteady aerodynamics of offshore floating wind turbines in platform pitching motion using vortex lattice method," *Renewable Energy*, 2014.

[27] Moore, K. R., and Ning, A., "Takeoff and performance trade-offs of retrofit distributed electric propulsion for urban transport," *Journal of Aircraft*, Vol. 56, No. 5, 2019, pp. 1880–1892.

[28] Lotsted, P., "Propeller Slip-Stream Model in Subsonic Linearized Potential Flow," *Journal of Aircraft*, Vol. 29, No. 6, 1992, pp. 1098–1105.

[29] Ehrich, S., Schwarz, C. M., Rahimi, H., Stoevesandt, B., and Peinke, J., "Comparison of the blade element momentum theory with computational fluid dynamics for wind turbine simulations in turbulent inflow," *Applied Sciences*, Vol. 8, No. 12, 2018, p. 2513.

[30] Catalano, F., and Stollery, J., "The effect of a high thrust pusher propeller on the flow over a straight wing," *11th Applied Aerodynamics Conference*, 1993, p. 3436.

[31] Chinwicharnam, K., and Thipyopas, C., "Comparison of wing-propeller interaction in tractor and pusher configuration," *International Journal of Micro Air Vehicles*, 2016.